

Optimizing Dynamic Performance of Virtual Synchronous Generator Based on Grid-connected Switching Control Strategy Using RBFNN Integrated Nonlinear Active Disturbance Rejection Control Approach

Yangyang Chen, Wei Han, Youhao Hu, Hanlei Tian, Yilin Zhang, and Junyu Fan

Abstract—The increasing use of distributed generation has revealed limitations in conventional power electronic converters, which are unable to provide sufficient inertia and damping support to the grid. As a result, virtual synchronous generator (VSG) has gained widespread adoption for regulating the output voltage and frequency. However, VSG may encounter challenges such as generating large inrush currents and power fluctuations during on-grid switching, significantly reducing the efficacy of virtual synchronous control strategies. Therefore, this study optimizes the dynamic performance of VSG based on grid-connected switching control strategy using radial basis function neural network (RBFNN) integrated nonlinear active disturbance rejection control (NLADRC) approach. In comparison with the conventional pre-synchronization control strategy, the proposed strategy effectively suppresses system variable oscillations through the NLADRC approach. This facilitates the rapid restoration of system output frequency, voltage, and power to the steady state, thereby enhancing transient stability. Moreover, the RBFNN-NLADRC approach leverages the robust fitting capability of the network for obtaining dynamic parameter information, which allows for gain parameter tuning, further enhancing the effectiveness of the proposed strategy. Finally, verifications conducted in MATLAB/Simulink and a Starsim hardware-in-the-loop environment illustrate the superiority and feasibility of the proposed strategy.

Index Terms—Virtual synchronous generator (VSG), nonlinear active disturbance rejection control (NLADRC), radial basis function neural network (RBFNN), grid-connected switching control.

Manuscript received: March 12, 2025; revised: June 8, 2025; accepted: September 22, 2025. Date of CrossCheck: September 22, 2025. Date of online publication: November 25, 2025.

This work was supported by Guangdong Basic and Applied Basic Research Fund (No. 2025A1515012012).

This article is distributed under the terms of the Creative Commons Attribution 4.0 International License (<http://creativecommons.org/licenses/by/4.0/>).

Y. Chen, W. Han (corresponding author), Y. Hu, H. Tian, Y. Zhang, and J. Fan are with The Hong Kong University of Science and Technology (Guangzhou), Guangzhou, China (e-mail: ychen981@connect.hkust-gz.edu.cn; weihan@hkust-gz.edu.cn; yhu543@connect.hkust-gz.edu.cn; thledu@ieee.org; yzhang775@connect.hkust-gz.edu.cn; jfan822@connect.hkust-gz.edu.cn).

DOI: 10.35833/MPCE.2025.000206

I. INTRODUCTION

THE utilization of distributed power generation technology has been identified as a crucial method to address the energy issues [1], [2]. Distributed power generation technology offers significant advantages in control mode and response speed compared with conventional power generation methods [3]. However, as the proportion of distributed energy increases, its inherent randomness and volatility have a greater impact on the system stability of the power grid. The conventional grid-connected interface control devices are unable to provide characteristics such as inertia and damping to the system [4]. To address this challenge, the virtual synchronous generator (VSG) enables the synchronization of the power supply of distributed inverter, allowing it to exhibit similar external characteristics to a synchronous generator and participate autonomously in power grid regulation. VSG has become widely recognized as an effective control technique for distributed power generation [5]-[7].

In general, VSG control strategies can be categorized into linear and nonlinear control strategies [8]-[10]. Regarding the linear control strategies, the proportional-integral (PI) controller remains widely used due to its simple structure and practicality [11], [12]. However, it fails to address the trade-off between speed and overshooting, and a single set of parameters cannot adapt to variable operation conditions. An effective approach to addressing the challenges is the active disturbance rejection control (ADRC) approach [13], [14]. This approach primarily utilizes extended state observers (ESOs) to identify aggregated uncertainties in the real-time system, effectively reducing unknown perturbations and enhancing the closed-loop stability of the system [15]. It is important to highlight that the implementation of ADRC approach does not necessitate the precise knowledge of the system model; it relies only on the measurement of a limited number of system states. Reference [16] introduces a framework for nonlinear ADRC (NLADRC) approach that employs nonlinear ESO (NLESO) to simplify the implementation process and enhance the feasibility of the analysis [16].

In [17]-[19], ADRC approach is applied to diverse control systems and demonstrates excellent control outcomes. However, the calibration of gain parameters of NLADRC approach presents a challenge in terms of complexity, which may hinder its widespread implementation and generalization in engineering applications.

Radial basis function neural network (RBFNN) algorithm has demonstrated significant success in the field of time series forecasting, attributed to their effectiveness in capturing nonlinear patterns [20]-[22]. A notable advantage of RBFNN algorithm over other neural network architectures is its capability to conveniently apply the orthogonal least square approach to construct a concise model, which exhibits excellent generalization performance [23], [24]. Employing such merits, numerous applications emerge including the positioning of robotics [25], link prediction [26], ultrasound localization microscopy [27], etc. In [28], the microgrid optimization model is introduced to quantify the dispatch elasticity as a demand response based on the time-of-use price of electricity, with the objective of minimizing the electricity cost for users and microgrid operation.

In addition, there are challenges for VSGs to achieve a seamless transition between islanded and grid-connected modes [29], [30]. Upon transitioning the VSG to on-grid operation modes, primary voltage regulation and frequency regulation are unable to entirely eliminate the voltage and frequency offsets. In severe cases, this situation may lead to transient shocks within the system [31], [32]. Recent research has explored various approaches for stability analysis and impedance estimation in power systems. Reference [33] presents a dynamic model for the online estimation of Thevenin's equivalent, demonstrating enhanced performance in both steady-state and transient tracking compared with frequency domain algorithms. However, this model encounters challenges when addressing time-varying systems and exhibits sensitivity to noise. In [34] and [35], the multi-input multi-output (MIMO) model is introduced for real-time impedance-based stability assessment, which effectively manages multiple inputs and outputs while providing rapid results suitable for adaptive control. Nevertheless, this model requires significant computation resources and exhibits a slow response to dynamic changes. To facilitate real-time impedance estimation in three-phase AC systems, digital twin technology has been employed alongside broadband excitation and Fourier techniques [36], achieving high precision but requiring high accuracy sensors and complex modeling. Additionally, [37] proposes an online continuous small signal stability monitoring approach for DC microgrids, which assesses stability margins without the need for additional hardware. However, this approach necessitates a comprehensive understanding of the system model and is less adaptable to nonlinear systems. Collectively, these studies offer valuable insights for improving VSG control strategy.

To address these challenges, this study optimizes dynamic performance of VSG based on grid-connected switching control strategy using RBFNN integrated NLADRC (RBFNN-

NLADRC) approach. Initially, the secondary frequency regulation of VSG is derived from the conventional VSG control strategy. Subsequently, to achieve difference-free frequency regulation of the system, a second-order NLADRC approach is integrated into the VSG control strategy based on the closed-loop transfer function. Furthermore, to tackle the challenge of gain parameter tuning of the NLADRC approach, the RBFNN algorithm is designed to optimize parameters, enhancing system control performance and addressing the parameter tuning difficulties. A concise summary of various approaches is presented in Supplementary Material A Table SAI. In summary, the proposed strategy offers several advantages over the existing strategies.

1) Compared with the pre-synchronization control strategy in [38], the VSG with the NLADRC approach omits the requirement for pre-synchronization, reducing voltage frequency oscillation at the time of grid-connection and achieving faster system response.

2) The introduction of the RBFNN algorithm addresses the parameter tuning difficulties of the NLADRC approach, which further ensures that the controller parameters are optimized, improving system output and enhancing system robustness.

3) The proposed strategy demonstrates exceptional performance in suppressing inrush current and power fluctuations, significantly improving the dynamic performance and transient stability of VSG under conditions of grid-connected switching and sudden three-phase frequency disturbances.

The remainder of this study is organized as follows. Section II outlines the basic principles of the VSG control strategy. Section III analyzes the control strategy for secondary frequency regulation of VSG. Section IV presents the design of the NLADRC approach. In Section V, the offline adaptation of RBFNN algorithm is introduced. Sections VI and VII present the simulation and experimental results, respectively. Finally, Section VIII offers the conclusion of this study.

II. BASIC PRINCIPLES OF VSG CONTROL STRATEGY

A. Modeling of VSG

The hardware configuration of the VSG closely resembles that of a conventional grid-connected inverter. This emulation is achieved by incorporating the mechanical and electromagnetic equations of a synchronous generator into the grid-connected inverter [39]. Figure 1 shows the block diagram of a grid-connected inverter employing VSG control strategy and power control loops on VSG, where LPF is short for low-pass filter, TD is short for tracking differentiator, and NLSEF is short for nonlinear state error feedback. To regulate the system, a voltage and current double closed-loop controller is employed, featuring a PI controller, which compares the reference voltage with the output voltage to generate the reference voltage V_o^* . Finally, a switching signal is generated using the space vector pulse width modulation (SVPWM), effectively implementing the control strategy.

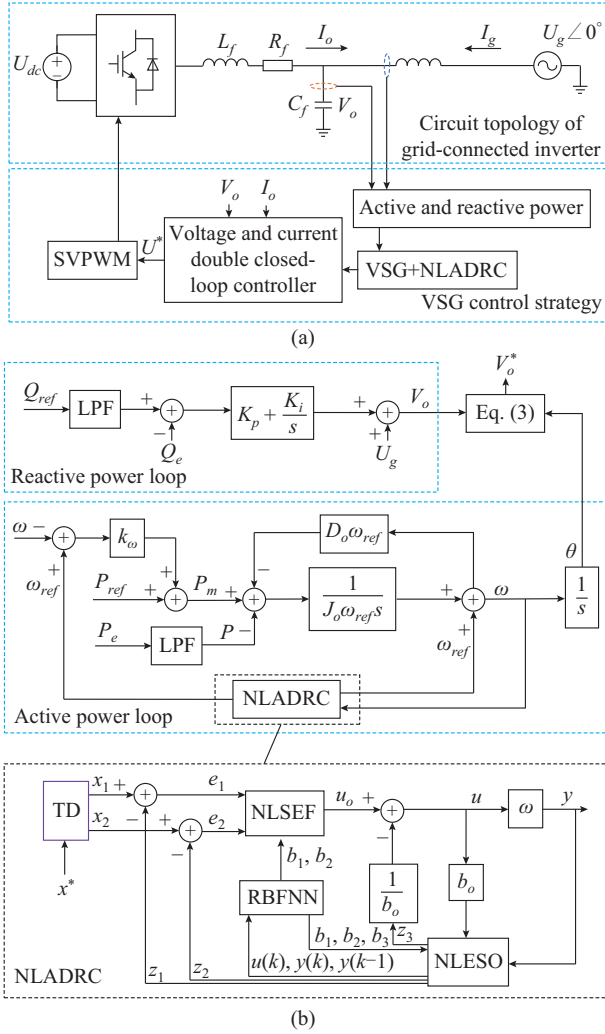


Fig. 1. Block diagram of a grid-connected inverter employing VSG control strategy and power control loops on VSG. (a) A grid-connected inverter employing VSG control strategy. (b) Power control loops on VSG.

B. Overall Control Structure of Conventional VSG Control Strategy

The conventional VSG control strategy is designed to incorporate P - f and Q - V control mechanisms, with the primary aim of delivering a predefined quantity of active and reactive power to the power grid. In practical scenarios, inherent harmonics in the control system, with a minimum frequency of twice the industrial frequency, will cause distortions in the output voltage. To mitigate this issue, LPF is integrated after the power measurement module to effectively filter the active power. This study introduces a novel derivation methodology. The state-space modeling of conventional VSG typically relies on direct linearization of mechanical equations without adequately considering the impact of LPFs in the power measurement module on system dynamics. This study models the relationship between the mechanical power and the active power by incorporating an LPF with a time constant, more accurately representing the filtering process of power signals in real control systems, thereby mitigating the dynamic bias associated with idealistic assumptions prevalent in conventional models. Therefore, the conventional

VSG control strategy can be formulated as:

$$\begin{cases} P = \frac{1}{\tau_e s + 1} P_e \\ P_m = k_\omega (\omega_{ref} - \omega) \\ P_m - P = J_o \omega_{ref} \frac{d\omega}{dt} - D_o \omega_{ref} (\omega - \omega_{ref}) \\ \theta = \int_0^t (\omega - \omega_{ref}) dt \end{cases} \quad (1)$$

$$V_o = U_g + \left(K_p + \frac{K_i}{s} \right) (Q_{ref} - Q_e) \quad (2)$$

where P and P_m are the mechanical and electromagnetic power, respectively; τ_e is the time constant of the LPF; P_e and Q_e are the active and reactive power outputs, respectively; ω is the output angular frequency; ω_{ref} is the reference angular frequency; J_o is the inertia coefficient; D_o is the damping coefficient; θ is the output power angle; V_o is the terminal voltage; U_g is the three-phase grid voltage; K_p is the proportional gain; k_ω is the droop gain of the P - f control loop; K_i is the integral gain; and Q_{ref} is the reference of reactive power. Note that V_o^* is determined by V_o and θ as shown in (3). Note that subscripts a , b , and c represent the three phases.

$$V_o^* = \begin{bmatrix} V_o \sin \theta \\ V_o \sin \left(\theta - \frac{2}{3} \pi \right) \\ V_o \sin \left(\theta + \frac{2}{3} \pi \right) \end{bmatrix} = \begin{bmatrix} V_{oa}^* \\ V_{ob}^* \\ V_{oc}^* \end{bmatrix} \quad (3)$$

As illustrated in Fig. 1, the closed-loop transfer function for the output angular frequency can be derived by (4), considering specific values for the active power and rated frequency.

$$\begin{cases} \omega = G_{P_{ref}} P_{ref} + G_P P + \omega_{ref} \\ G_{P_{ref}} = \frac{1}{J_o \omega_{ref} s + (D_o + k_\omega) \omega_{ref}} \\ G_P = \frac{1}{[J_o \omega_{ref} s + (D_o + k_\omega) \omega_{ref}] (\tau_e s + 1)} \end{cases} \quad (4)$$

The time domain expression of (4) can be derived by Laplace inverse transformation as:

$$\frac{d^2 \omega}{dt^2} = - \frac{[J_o \omega_{ref} + (D_o + k_\omega) \omega_{ref} \tau_e]}{J_o \omega_{ref} \tau_e} \frac{d\omega}{dt} - \frac{D_o + k_\omega}{J_o \tau_e} \omega + \frac{P_{ref} - P}{J_o \omega_{ref} \tau_e} + \frac{D_o + k_\omega}{J_o \tau_e} \omega_{ref} \quad (5)$$

III. CONTROL STRATEGY FOR SECONDARY FREQUENCY REGULATION OF VSG

The conventional VSG control strategy enables real-time adjustment of its output to provide frequency support for the power grid. However, this strategy is limited to the primary frequency regulation function and is unable to ensure power quality in isolated states. Consequently, there is a pressing

need for further research to develop a control strategy for secondary frequency regulation of VSG that can enhance the stability and performance of VSG system.

From (1), when the system is under steady-state operation, we can obtain:

$$\frac{P_m - P}{\omega_{ref}} = D_o(\omega - \omega_{ref}) \quad (6)$$

As illustrated in Fig. 2, the system operates at an initial equilibrium point A , which represents the intersection of the generator characteristic curve (represented by P_{G1}) and the load characteristic curve (represented by P_{L1}). The system frequency is denoted as f . Upon a load increase of ΔP_L , the load characteristic curve shifts upwards, while the generator characteristic curve remains unchanged. Consequently, the stable operation point transitions to point B , accompanied by a corresponding change in the stable operation frequency to f' . As a result, the motor power increases by ΔP_G . In line with the principle of secondary frequency regulation, it becomes imperative to shift the generator characteristic curve to P_{G2} , thereby facilitating the attainment of a new stable operation point, denoted as point C , and the operation frequency of the system is f'' [40]. At this juncture, the secondary frequency regulation formula of VSG can be derived in accordance with the principle of secondary frequency regulation, as shown in (7). In the context of the secondary frequency regulation of VSG, ΔP_m and ΔP represent the incremental mechanical and electromagnetic power, respectively. It is imperative to note that the attainment of $\Delta P_m = \Delta P$ is essential for achieving $\Delta f = 0$, signifying the nondifferential frequency regulation.

$$\Delta f = \frac{\Delta P_m - \Delta P}{2\pi D_o \omega_{ref}} \quad (7)$$

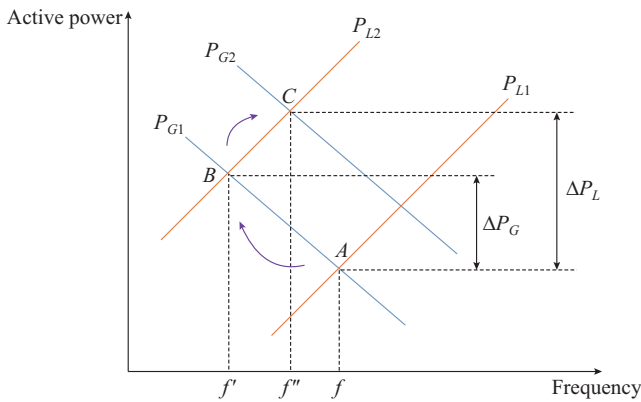


Fig. 2. Principle of dynamic characteristics for secondary frequency regulation of VSG.

IV. DESIGN OF NLADRC APPROACH

The structure of the NLADRC approach for VSG, as shown in Fig. 1, consists of three components: TD, NLSEF, and NLESO [41]. Before employing the NLADRC approach, the VSG system is firstly modelled as a standard second-order system as:

$$\begin{cases} x_1 = y = \omega \\ \dot{x}_1 = x_2 = \dot{\omega} \\ \dot{x}_2 = f(x_1, x_2, w) + w + b_o u = \dot{x}_3 + b_o u \\ \dot{x}_3 = f(x_1, x_2, w) + w \end{cases} \quad (8)$$

$$\begin{cases} f(x_1, x_2, w) = -\frac{J_o \omega_{ref} + (D_o + k_\omega) \omega_{ref} \tau_e}{J_o \omega_{ref} \tau_e} \frac{d\omega}{dt} - \\ \frac{D_o + k_\omega}{J_o \tau_e} \omega + \frac{P_{ref} - P_e}{J_o \omega_{ref} \tau_e} \\ b_o = \frac{D_o + k_\omega}{J_o \tau_e} \\ u = \omega_{ref} \end{cases} \quad (9)$$

where x_1 and x_2 are the state variables; y is the output of the system; w is the unknown external disturbance affecting the system; $f(x_1, x_2, w)$ is the dynamic characteristic function; b_o is the control gain; \dot{x}_3 is the cumulative effect of both internal and external disturbances within the system; and u is the control input. The analysis of (8) and (9) reveals the significant impact of the power output value on the stability performance of the NLADRC approach. While the power output value is a key factor in the disturbance, it is just one element of a broader range of factors affecting stability, including discrepancies between specified and actual power output values, system angular frequency, and unmodeled frequency deviations. By accurately addressing and compensating for these combined disturbances, an integrator series structure can be established. This capability allows the NLADRC approach to effectively track reference signals without overshoots or deviations, showcasing its advantage of not requiring a precise model of the controlled system. Denoting $v(k)$ as the input signal, and $x_1(k)$ and $x_2(k)$ as the estimation of ω and its first derivative, the TD for VSG is designed as in (10) and (11).

$$\begin{cases} e(k) = x_1(k) - v(k) \\ x_1(k+1) = x_1(k) + h_o x_2(k) \\ x_2(k+1) = x_2(k) + h_o f_{han}(e_1(k), x_2(k), r, h_o) \end{cases} \quad (10)$$

$$\begin{cases} \eta = h_o r \\ \eta_o = r h_o^2 \\ y = x_1 + h_o x_2 \\ a_o = \sqrt{8r|y| + \eta^2} \\ f_{sg}(a, b) = \frac{\text{sign}(a+b) - \text{sign}(a-b)}{2} \\ a_1 = \frac{h_o x_2 + y}{h_o} f_{sg}(y, \eta_o) + \\ \frac{2x_2 + (a_o - \eta) \cdot \text{sign}(y)}{2} (1 - f_{sg}(y, \eta_o)) \\ f_{han} = -r \frac{a_1}{\eta} f_{sg}(a_1, \eta) - r \text{sign}(a_1) \cdot (1 - f_{sg}(a_1, \eta)) \end{cases} \quad (11)$$

where $e(k)$ is the error between the actual output and the discriminative output; h_o is the integration step; r is the

speed factor; $f_{han}(\cdot)$ is the fastest tracking function; and $f_{sg}(a, b)$ is the switch function utilized for smooth transitions.

Note that a proper design of TD for VSG guarantees swift and accurate tracking behaviors of VSG system in accordance with the established transition process and reference instructions, thereby enhancing the overall control performance of the system.

To estimate the lumped disturbance in the VSG system, a third-order NLESO is constructed as:

$$\begin{cases} e_3 = z_1 - \omega \\ \dot{z}_1 = z_2 - b_1 f_{al}(e_2, \alpha_1, \delta) \\ \dot{z}_2 = z_3 - b_2 f_{al}(e_2, \alpha_1, \delta) + b_o \omega_{ref} \\ \dot{z}_3 = -b_3 f_{al}(e_2, \alpha_2, \delta) \end{cases} \quad (12)$$

$$f_{al}(a, b, c) = \frac{a}{c^{1-b}} (1 - f_{sg}(|a|, c)) + |a|^b \cdot \text{sign}(a) \cdot f_{sg}(|a|, c) \quad (13)$$

where e_3 is the tracking error; b_1 , b_2 , and b_3 are the nonlinear gain coefficients; α_1 and α_2 are the factors of the nonlinear segment interval; δ is the length of the nonlinear interval; and z_1 , z_2 , and z_3 are the output, derivative value of the output, and estimation of the total perturbation of the controlled object, respectively.

Finally, NLSEF composed of states of TD and NLESO is designed as:

$$\begin{cases} e_1 = x_1 - z_1 \\ e_2 = x_2 - z_2 \\ u_0 = b_1 f_{al}(e_1, \alpha_2, \delta) + b_2 f_{al}(e_2, \alpha_3, \delta) \\ u = u_0 - \frac{z_3}{b_o} \end{cases} \quad (14)$$

where α_3 is equivalent to α_1 and α_2 and serves as a factor of the nonlinear segment interval.

The features of the NLADRC approach can be listed as follows.

1) It eliminates the need for precise system modeling of VSG system, enabling rapid response and accurate tracking by actively countering disturbances.

2) Its integration into the secondary frequency regulation significantly improves the speed and effectiveness of system frequency regulation.

3) It enhances the VSG control strategy and increase the system resistance to various disturbances through real-time disturbance estimation and compensation, thus strengthening the system robustness against internal and external uncertainties.

V. OFFLINE ADAPTATION OF RBFNN ALGORITHM

In this section, the gain parameters in the NLADRC approach are optimized by the RBFNN algorithm, exhibiting excellent self-learning capability in nonlinear system.

A. RBFNN Algorithm

The RBFNN algorithm comprises a three-layer feed-forward neural network structure, as shown in Fig. 3. The input

signal neuron nodes form the first layer with the number of neurons determined based on the dimensions of the input data. The second layer represents the hidden layer, which can abstract the input layer space to a higher dimensional space and classify different data types. The activation function chosen for this layer is the Gaussian function. The Gaussian function $\phi_l(x)$ is widely used due to its strong performance, which compares the similarity between the input vector and the center of the hidden node, and can be expressed as:

$$\phi_l(x) = \exp\left(-\frac{\|X - c_l\|^2}{2\sigma_l^2}\right) \quad l = 1, 2, \dots, e \quad (15)$$

where $X = [x_1, x_2, \dots, x_N]$ is the input vector of the network; l is the number of hidden layer neurons; $c_l = [c_{l1}, c_{l2}, \dots, c_{lN}]$ is the Gaussian centroid of the first hidden layer neuron; σ_l is the base width length of the l^{th} hidden layer node; and $\|\cdot\|$ is the Euclidean vector norm.

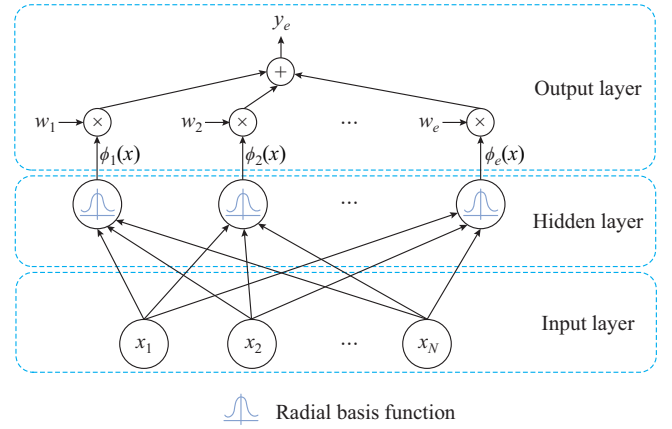


Fig. 3. Structure of RBFNN algorithm.

The third layer (the output layer) is formed after weighing the output of the hidden layer. The expression of the output layer is given as:

$$y_e = \mathbf{w}_l^T \boldsymbol{\phi}(x) = w_1 \phi_1(x) + w_2 \phi_2(x) + \dots + w_e \phi_e(x) \quad (16)$$

where $\mathbf{w}_l = [w_1, w_2, \dots, w_e]^T$ is the weight vector of the output layer; and $\boldsymbol{\phi}(x) = [\phi_1(x), \phi_2(x), \dots, \phi_e(x)]^T$ is the output vector of the hidden layer.

The input layer receives input data and transmits the data directly to the hidden layer. In the hidden layer, each neuron calculates the similarity between the input vector and its corresponding center using a Gaussian function. This similarity measure determines the activation value of each hidden layer neuron. The output of the Gaussian function is maximized when the input vector is close to the neuron center and diminishes as the distance from the center increases.

Subsequently, the outputs from the hidden layer neurons are weighted and summed in the output layer to generate the final output. The weights in the output layer dictate the contribution of each hidden layer neuron to the overall output. The training process of the RBFNN algorithm primarily focuses on determining the centers and widths of the hidden layer neurons, as well as the weights for the output layer. By

employing suitable training algorithms, the network can effectively learn the relationship between input and output data, facilitating function approximation.

B. Parameter Tuning of NLADRC Approach

In this subsection, the error between the fitted output and the desired output is utilized to train the network parameters, thereby enhancing network accuracy. Based on this, the neural network model of VSG angular velocity variation is obtained through online identification, enabling parameter tuning of the NLADRC approach.

For the current sampling moment k of the system, the performance indicator function $E(k)$ is calculated as:

$$E(k) = \frac{1}{2} (y(k) - y_e(k))^2 = \frac{1}{2} (e(k))^2 \quad (17)$$

where $y(k)$ is the actual output of the system; and $y_e(k)$ is the discriminative output of the RBFNN algorithm.

The mapping function of neural network must be trained to minimize the tracking errors. This involves determining the parameters of the basis function for c_l , σ_l and the weight coefficient w_{ij} . In this study, the gradient descent approach is employed to learn and train the network model parameters [42], with the specific training formulas as:

$$\begin{cases} \Delta w_{ij}(k) = -\lambda \frac{\partial E(k)}{\partial w_{ij}(k-1)} = \lambda e_j(k) \phi_l(\mathbf{x}(k)) \\ w_{ij}(k) = w_{ij}(k-1) + \Delta w_{ij}(k) + \alpha (w_{ij}(k-1) - w_{ij}(k-2)) \end{cases} \quad (18)$$

$$\begin{cases} \Delta c_l(k) = -\lambda \frac{\partial E(k)}{\partial c_l(k-1)} = \lambda e_j(k) w_{ij}(k-1) \phi_l(\mathbf{x}(k)) \cdot \frac{\mathbf{x}(k) - c_l(k-1)}{\sigma_l^2(k-1)} \\ c_l(k) = c_l(k-1) + \Delta c_l(k) + \alpha (c_l(k-1) - c_l(k-2)) \end{cases} \quad (19)$$

$$\begin{cases} \Delta \sigma_l(k) = -\lambda \frac{\partial E(k)}{\partial \sigma_l(k-1)} = \lambda e_j(k) w_{ij}(k-1) \phi_l(\mathbf{x}(k)) \cdot \frac{(\mathbf{X}(k) - c_l(k-1))^2}{\sigma_l^3(k-1)} \\ \sigma_l(k) = \sigma_l(k-1) + \Delta \sigma_l(k) + \alpha (\sigma_l(k-1) - \sigma_l(k-2)) \end{cases} \quad (20)$$

where $j=1,2,\dots,N$; $\mathbf{x}(k)$ is the actual input of the system; $\Delta w_{ij}(k)$ is the increment of the weight coefficient; $\Delta c_l(k)$ is the increment of the Gaussian centroid vector; $\Delta \sigma_l(k)$ is the increment of Gaussian function width; $\mathbf{X}(k) = [u(k), y(k), y(k-1)]^T$ is the input vector of the RBFNN algorithm; λ is the learning rate, which is constrained to the range $[0, 1]$; and α is the momentum factor.

The incremental coefficients for the three parameters b_1 , b_2 , b_3 in NLESO are defined as:

$$\begin{cases} e_{c1}(k) = e(k) - e(k-1) \\ e_{c2}(k) = e(k) \\ e_{c3}(k) = e(k) - 2e(k-1) + e(k-2) \end{cases} \quad (21)$$

$$\begin{cases} b_1 = b_1(k-1) + b_1(k-1)e(k) \frac{\partial y(k)}{\partial u(k)} e_{c1}(k) \\ b_2 = b_2(k-1) + b_2(k-1)e(k) \frac{\partial y(k)}{\partial u(k)} e_{c2}(k) \\ b_3 = b_3(k-1) + b_3(k-1)e(k) \frac{\partial y(k)}{\partial u(k)} e_{c3}(k) \end{cases} \quad (22)$$

where $e_{c1}(k)$, $e_{c2}(k)$, and $e_{c3}(k)$ are the error increment terms; $\partial y(k)/\partial u(k)$ is the Jacobian information of the controlled object.

The RBFNN algorithm can obtain dynamic quantity, specifically Jacobian information, following the acquisition of the fitted output of the recognized object. Based on the preceding analysis, it is evident that the neural network will yield $y_e(k)$ after training, with an exceedingly small recognition error. This allows for the consideration that $y_e(k)$ is equivalent to $y(k)$. Consequently, we can obtain:

$$\frac{\partial y(k)}{\partial u(k)} \approx \frac{\partial y_e(k)}{\partial u(k)} = \sum_{l=1}^M w_{ij}(k-1) \phi_l(\mathbf{x}(k)) \frac{c_l(k-1) - u(k)}{\sigma_l^2(k-1)} \quad (23)$$

The training flow chart of the RBFNN algorithm is shown in Fig. 4. The input signal $u(k)$ and the real-time output signals $y(k)$ and $y(k-1)$ of the inverter are collected as the neuron signals of the input layer of the neural network. After training, $y_e(k+1)$ is discerned, and the error between the actual output of the angular velocity and the discerned output is used to correct the internal parameters of the neural network until the set error index is satisfied. After that, the learned neural network is utilized to optimize the gain parameters in the controller in real time. $y_e(k+1)$ is used under the error index instead of the actual angular velocity of the inverter $y(k-1)$ to determine the output corresponding to the input of the bias conductor. This bias conductor can provide increments, enabling the adjustment of the gain parameters.

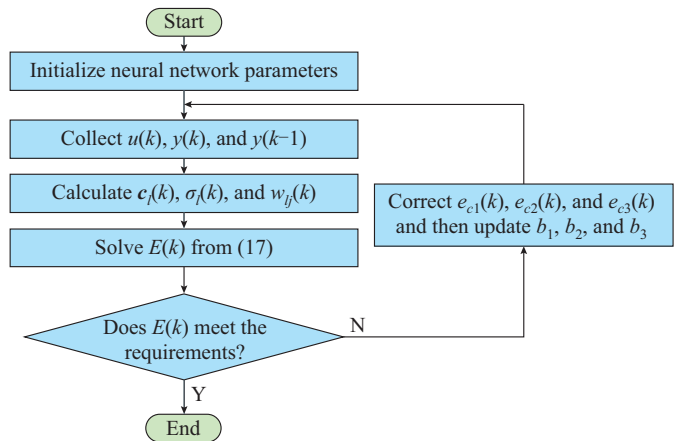


Fig. 4. Training flow chart of RBFNN algorithm.

VI. SIMULATION RESULTS

In this section, a MATLAB/Simulink model for VSG is developed with system parameters in [43] to assess the efficacy of the proposed strategy. The detailed parameters of

VSG system are listed in Table I.

TABLE I
PARAMETERS OF VSG SYSTEM

Parameter	Value	Parameter	Value
DC-side voltage U_{dc}	800 V	Line resistance R_g	0.8 m Ω
Grid frequency f_g	50 Hz	Line inductor L_g	15 mH
Filter capacitor C_f	0.2 μ F	Local load P_L	6 kW
Parasitic resistance R_f	0.2 Ω	$\alpha_1, \alpha_2, \alpha_3$	0.5, 0.25, 1.2
Filter inductor L_f	5 mH	c	10^{-3}
Reference of active power P^*	10 kW	r	5^3
D_o	10	b_1, b_2, b_3	$10^7, 10^2, 10^5$
U_g	311 V	h_o	10^{-4}
J_o	0.3	θ	10^{-3}

To address the challenge of substantial inrush current associated with conventional switching curves under operation mode, an innovative pre-synchronization process is introduced, which is based on voltage and frequency compensation signals derived from the conventional VSG control strategy in the simulation structure [44]. By effectively mitigating the instantaneous inrush current during the synchronization period, this pre-synchronization process has been incorporated as one of the cases in the simulation results. The simulation includes four cases as follows.

A. Case 1: VSG with Pre-synchronization Control Strategy

The simulation results of Case 1 are shown in Figs. 5-7, where V_{VSG} and V_g are the magnitudes of output voltage of VSG with pre-synchronized control strategy and power grid, respectively; f_{VSG} and f_g are the frequencies of VSG with pre-synchronized control strategy and power grid, respectively; and I_{VSG} and I_g are the output currents of VSG with pre-synchronized control strategy and power grid, respectively. Before transitioning the VSG from islanding mode to grid-connected mode, it is initially connected to the local load at $t=0.2$ s, followed by the execution of the pre-synchronization process at $t=0.5$ s. Subsequently, the grid-connection signal is issued at $t=0.7$ s, resulting in the successful connection of the VSG to the grid. As shown in Fig. 5, the active power undergoes a change from the 6 kW load already carried to the rated power of 10 kW. However, with the pre-synchronization control strategy, only approximately 9.8 kW output power can be reached. The settling time is 0.45 s with a 3% error band.

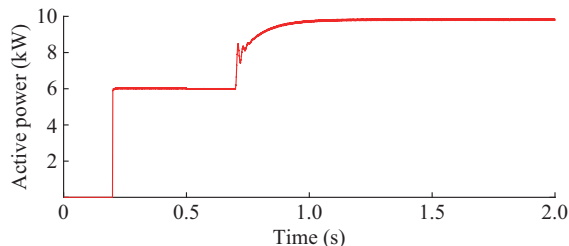


Fig. 5. Active power supplied by VSG with pre-synchronization control strategy.

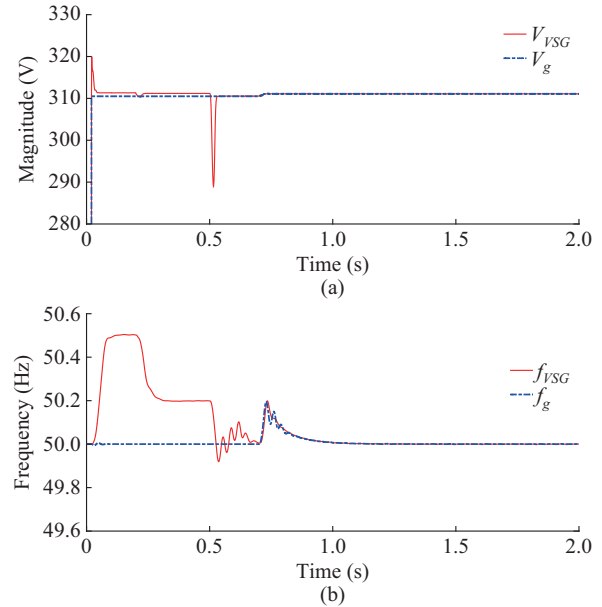


Fig. 6. Magnitudes of output voltages and frequencies of VSG with pre-synchronization control strategy and power grid. (a) Magnitude. (b) Frequency.

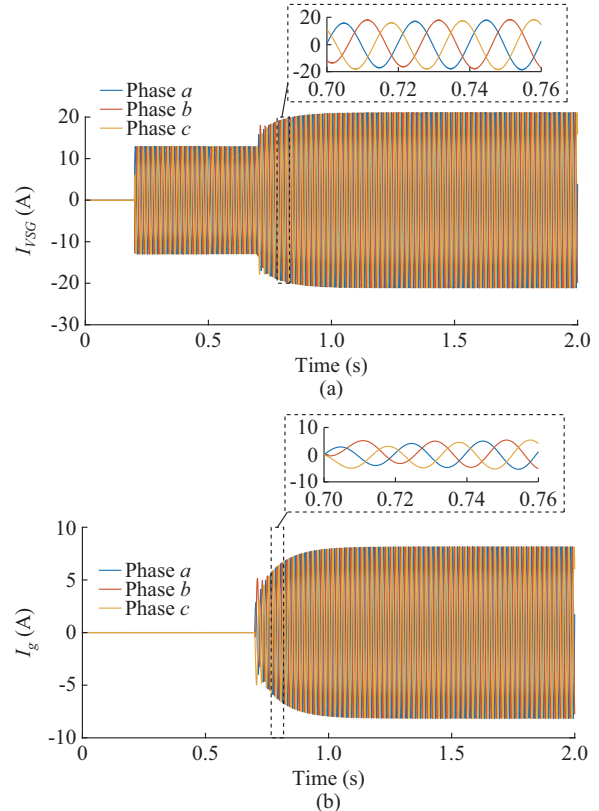


Fig. 7. Output currents of VSG with pre-synchronization control strategy and power grid. (a) Output current of VSG with pre-synchronization control strategy. (b) Output current of power grid.

In Fig. 6(a), at the commencement of the pre-synchronization, the presence of a phase difference causes a shock in the active power, with the magnitude being restored to the normal value through voltage compensation. The magnitude

after grid connection increases to some extent due to inverter supplementation and stabilizes at around 311 V. Additionally, Fig. 6(b) indicates that before the local load connection, the frequency of the VSG is high, reaching 50.5 Hz. After the local load connection, the frequency decreases to around 50.2 Hz. The variation in the frequency of the VSG observed during the pre-synchronization period (0.5-0.7 s) is attributed to the effect of the PI regulator, with the frequency quickly returning to near the nominal value due to frequency compensation. Following grid connection, the frequency returns to the nominal value at $t=0.8$ s, despite the initial slight deviation. With secondary frequency regulation, the frequencies of the VSG and the power grid are perfectly matched. Based on the observations from Fig. 7, it is evident that no inrush current is observed after the transition, although current waveform distortion remains present.

B. Case 2: VSG with NLADRC Approach

The simulation results of Case 2 are shown in Figs. 8-10. In Case 2, the VSG is connected to $P_L=6$ kW at $t=0.2$ s and subsequently increases to $P_N=10$ kW after grid connection at $t=0.5$ s. The active power supplied by VSG with the NLADRC approach is presented in Fig. 8. The simulation results indicate that the ADRC controller adjusts the system according to the power increase without affecting stability, similar to the pre-synchronization control strategy in terms of the adjustment effect. However, it eliminates the need for the pre-synchronization process. With the settling time reduced to 0.21 s and consideration of a 3% error band, the self-resilient control demonstrates fast convergence.

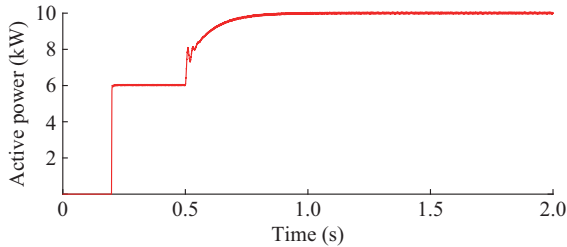


Fig. 8. Active power supplied by VSG with NLADRC approach.

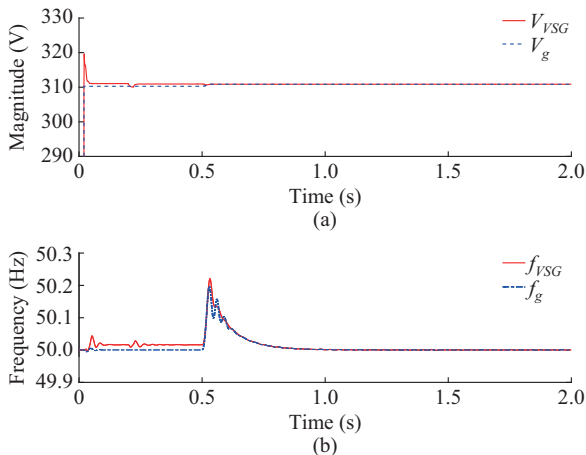


Fig. 9. Magnitudes of output voltages and frequencies of VSG with NLADRC approach and power grid. (a) Magnitude. (b) Frequency.

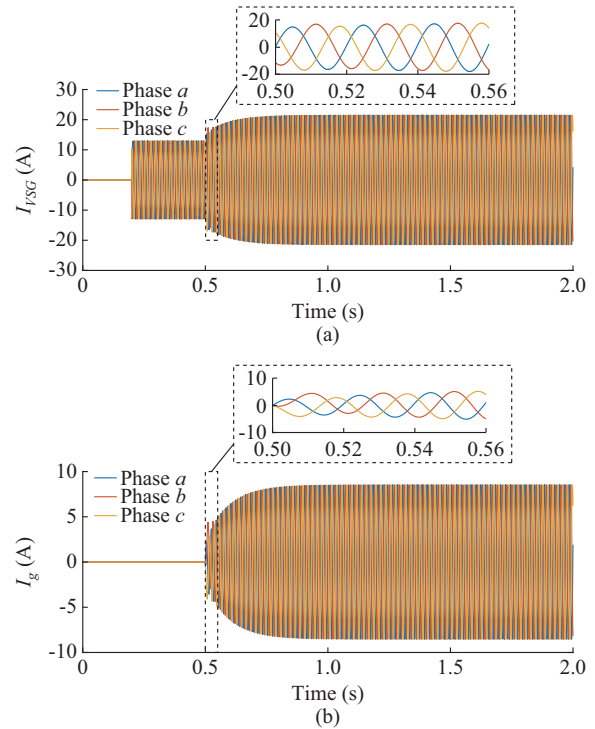


Fig. 10. Output currents of VSG with NLADRC approach and power grid. (a) Output current of VSG with NLADRC approach. (b) Output current of power grid.

Figure 9 presents the magnitudes of output voltages and frequencies of VSG with the RBFNN-NLADRC approach and power grid. It is observed that the magnitude remains relatively constant during the simulation, and the transient magnitude during the pre-synchronization period is resolved. Additionally, the frequency is approximately 50.01 Hz before grid connection, and the frequency variation after grid connection is substantially reduced in the oscillation time compared with that in Case 1. The highest frequency in the transient process is around 50.2 Hz, signifying the stable operation of the power grid and provision of a safe and uninterrupted power supply. However, the current waveform distortion in Fig. 10 remains presenting a similar effect to that of the pre-synchronized control strategy. Further research is needed in the parameter tuning of the NLADRC approach to comprehensively optimize the VSG system characteristics based on the simulation results.

C. Case 3: VSG with RBFNN-NLADRC Approach

The simulation results of Case 3 are shown in Figs. 11-13 and Supplementary Material A Figs. SA1-SA3.

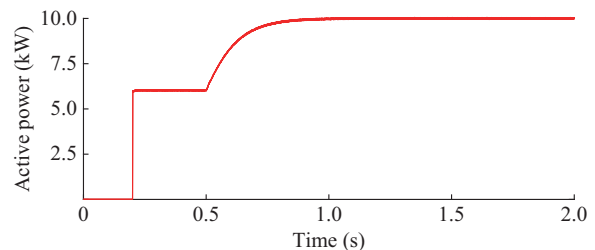


Fig. 11. Active power supplied by VSG with RBFNN-NLADRC approach.

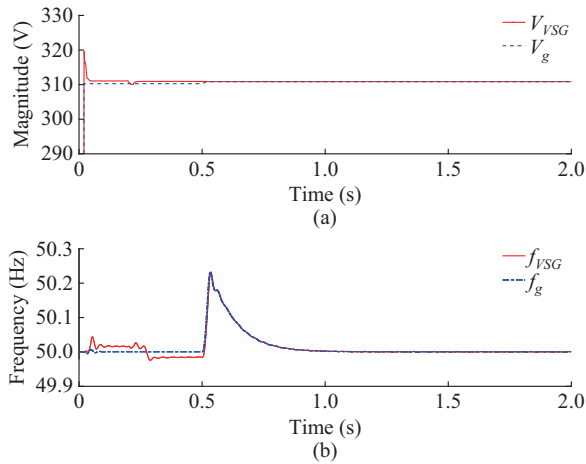


Fig. 12. Magnitudes of output voltages and frequencies of VSG with RBFNN-NLADRC approach and power grid. (a) Magnitude. (b) Frequency.

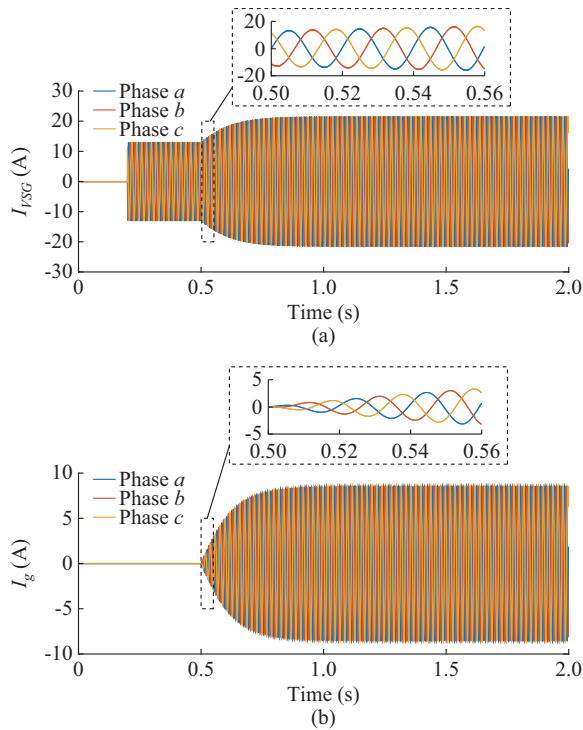


Fig. 13. Output currents of VSG with RBFNN-NLADRC approach and power grid. (a) Output current of VSG with RBFNN-NLADRC approach. (b) Output current of power grid.

In Case 3, the islanding and grid-connected switching of the VSG mirrors that of Case 2 by substituting $b_1=300025$, $b_2=28.00023$, and $b_3=3000.25$ into the NLADRC approach, based on the findings presented in Supplementary Material A Fig. SA2. In Fig. 11, despite the settling time increasing to 0.24 s compared with the NLADRC approach, the perturbation of the transient process has been eliminated. The change of the active power throughout the grid-connection process is notably smooth, with a significant reduction in both the response and adjustment time, providing compelling evidence of the effectiveness of the proposed strategy. In Fig. 12, similar results are illustrated to those observed for the magnitude in Case 2. Notably, with the adoption of RBFNN algorithm,

the frequency is reduced to around 49.98 Hz at $t=0.25$ s, within the acceptable range of the power grid. Additionally, the transient tracking of frequency at 0.5 s is observed when the grid-connection signal is issued, combined with the ability to respond better to system variations due to the inclusion of RBFNN algorithm in the NLADRC approach. In Fig. 13, the simulation results of the output current are presented, indicating the complete suppression of current distortion.

The superiority of the proposed strategy can be summarized as follows.

1) The NLADRC approach facilitates system adjustment from islanding mode to grid-connected mode without compromising stability, which shares similarities with pre-synchronized control strategy in terms of adjustment effectiveness but eliminates the pre-synchronization process while demonstrating rapid convergence.

2) The RBFNN algorithm exhibits robust nonlinear approximation capabilities, enabling it to derive optimal gain parameter solutions in response to variations in gain parameters with the NLADRC approach during the operation of the VSG system.

3) Upon completion of the training process, the RBFNN algorithm utilizes the error between the actual and predicted outputs of the angular velocity to adjust its internal parameters, which effectively minimizes frequency variations within the acceptable limits of the VSG, thereby mitigating disturbances and waveform distortions during transient events associated with grid connection.

Figure 14 presents the harmonic analysis and total harmonic distortion (THD) performance for Cases 1-3. In Case 1, the magnitude of lower harmonics (e.g., 5th, 7th, and 11th) is relatively high and exhibits a gradual decrease with increasing harmonic order. Higher harmonics (e.g., 50th and above) display lower magnitudes. In Case 2, the magnitudes of lower harmonics are significantly reduced, and the trend of harmonic attenuation is more pronounced. In Case 3, the magnitudes of both lower and higher harmonics are further suppressed, with a more rapid attenuation observed. This marginal reduction, compared with that with the NLADRC approach, indicates that the introduction of the RBFNN algorithm in conjunction with the NLADRC approach leads to improved harmonic suppression and a lower THD, yielding a lower THD and the optimization of power quality.

To facilitate a more effective comparison of the steady-state error of active power and the THD of the output current across the three cases, Table II presents a comparison of control performance during grid-connected transitions. Under the pre-synchronization control strategy, the steady-state error of active power is recorded at 1.60%, while the THD of output current is 1.78%. When the NLADRC approach is implemented, the steady-state error of active power decreases to 0.61%, reflecting an improvement of 0.99%. Additionally, the THD of output current is reduced to 0.91%, indicating an improvement of 0.87%. Furthermore, the RBFNN-NLADRC approach further decreases the steady-state error of active power to 0.40% and the THD to 0.85%, yielding respective improvements of 0.21% and 0.06% compared with the NLADRC approach.

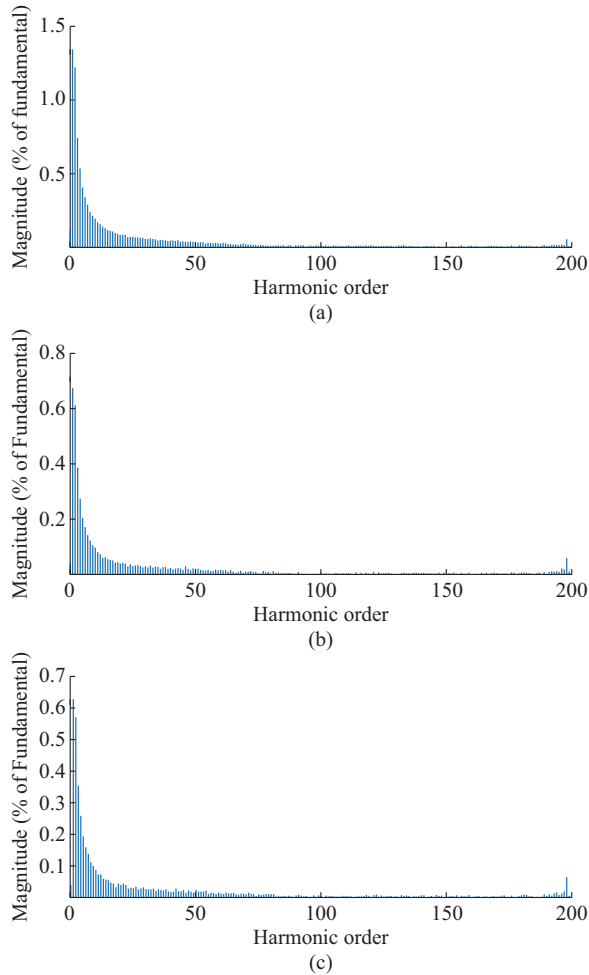


Fig. 14. Harmonic analysis and THD performance for Cases 1-3. (a) Case 1. (b) Case 2. (c) Case 3.

TABLE II
COMPARISON OF CONTROL PERFORMANCE DURING GRID-CONNECTED TRANSITIONS

Case	Steady-state error of active power (%)	THD of output current (%)
Case 1	1.60	1.78
Case 2	0.61	0.91
Case 3	0.40	0.85

D. Case 4: VSG with Frequency Disturbances

Based on the previous three cases, the frequency of the three phases changes from 50 Hz to 49.5 Hz at 1.2 s after the VSG is connected to the power grid. Figure 15 shows the active power supplied by VSG in Cases 1-3. In Fig. 15 (a), the active power initially experiences a sharp decline to approximately -27 kW before rebounding quickly, exhibiting an oscillation degree, and gradually stabilizing after 1.41 s. This behavior indicates that, under pre-synchronization control strategy, the system is significantly affected by frequency disturbances, resulting in substantial power fluctuations.

In Fig. 15(b), the decrease in the active power magnitude is relatively modest, with the lowest point being higher than

that observed in Fig. 15(a). This suggests that the NLADRC approach has enhanced the system resilience to frequency disturbances, thereby improving its dynamic performance and stability. In Fig. 15(c), the addition of faults results in further mitigation of power fluctuations. The decrease in the active power magnitude is minimal, and the system returns to a stable state within 1.2 s post-decrease. This outcome highlights the superiority of the RBFNN-NLADRC approach, as the incorporation of RBFNN algorithm enhances the robustness and adaptability of the system, allowing it to maintain active power stability more effectively in the presence of frequency disturbances. Supplementary Material A Fig. SA4 illustrates the performance indicator function.

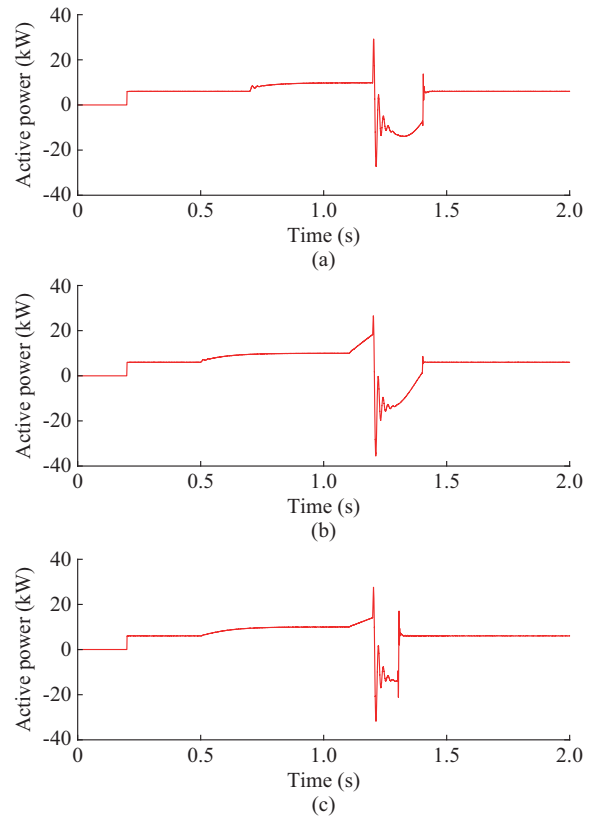


Fig. 15. Active power supplied by VSG under Cases 1-3. (a) Case 1. (b) Case 2. (c) Case 3.

VII. EXPERIMENTAL RESULTS

To further validate the feasibility of the proposed strategy. This study also conducts a Starsim hardware-in-the-loop (HIL) test, providing an advanced model-based framework for the interaction with real-world scenarios. A real-time simulator (MT6060) is utilized to replicate the power stage, while a rapid control prototype (MT1070) functions as a dynamic development platform for in-lab verification of the VSG control strategy. The experimental setup, as shown in Supplementary Material A Fig. SA5, entails the real-time simulator replicating the behavior of loads, semiconductor switches, and their associated driver circuits. Meanwhile, the rapid control prototype acquires the output parameters of real-time simulator, encompassing grid frequency, current, voltage, and power metrics, and synthesizes the control signals

at a 25 μ s sampling interval.

In order to demonstrate the effectiveness of the proposed strategy, the simulation program detailed in Section VI is replicated to obtain experimental results. The parameters of the experiment are set to match those used in the simulation, allowing for a feasible comparison between simulation and experimental results. The results shown in Supplementary Material A Fig. SA6 illustrate a high degree of congruence between the experimental outcomes of the proposed strategy and the simulation results, indicating the consistency across both modalities. The consistency observed demonstrates the effectiveness of the NLADRC approach and RBFNN-NLADRC approach in facilitating a seamless transition between islanding mode and grid-connected mode. Specifically, in Supplementary Material A Fig. SA6, the trace in blue represent the active power signals for the VSG with pre-synchronization control strategy, while the green and orange traces denote the VSG with the NLADRC approach and RBFNN-NLADRC approach, respectively.

VIII. CONCLUSION

This study optimizes dynamic performance of VSG based on grid-connected switching control strategy using RBFNN-NLADRC approach. Moreover, to address the challenge of parameter tuning, the RBFNN algorithm is utilized for adjustment of key controller parameters, further enhancing the system anti-interference capability. Simulation and experimental results demonstrate the effectiveness in reducing system response time and suppressing oscillations, thereby enhancing the dynamic performance and stability of the VSG system. Future research will concentrate on enhancing the RBFNN algorithm or optimizing it with other parameter learning algorithms. In multi-machine VSG scenarios [44], the RBFNN-NLADRC approach can be integrated with node sensitivity assessment to prioritize and optimize the control parameters of vulnerable nodes. This approach enhances system efficiency while maintaining stability. Additionally, the investigation will extend to cooperative control strategies that involve energy storage systems, photovoltaic sources, and the grid within the VSG framework.

REFERENCES

- [1] C. C. Chan, W. Han, H. Tian *et al.*, "Automotive revolution and carbon neutrality," *Frontiers in Energy*, vol. 17, no. 6, pp. 693-703, Oct. 2023.
- [2] Y. Chen, W. Han, Y. Hu *et al.*, "Adaptive control for improved virtual synchronous generator under imbalanced grid voltage," *IEEE Open Journal of the Industrial Electronics Society*, vol. 5, pp. 722-736, Jul. 2024.
- [3] Ê. C. Resende, M. G. Simões, and L. C. G. Freitas, "Anti-islanding techniques for integration of inverter-based distributed energy resources to the electric power system," *IEEE Access*, vol. 12, pp. 17195-17230, Jan. 2024.
- [4] H. Tian, G. Liang, M. Chen *et al.*, "An integrated flyback rectifier with power decoupling and auto PFC," *IEEE Journal of Emerging and Selected Topics in Power Electronics*, vol. 12, no. 2, pp. 1883-1893, Apr. 2024.
- [5] Z. Wang, Y. Yu, W. Gao *et al.*, "Adaptive, optimal, virtual synchronous generator control of three-phase grid-connected inverters under different grid conditions: an adaptive dynamic programming approach," *IEEE Transactions on Industrial Informatics*, vol. 18, no. 11, pp. 7388-7399, Nov. 2022.
- [6] Y. Ma, J. Xu, C. Gao *et al.*, "Low-frequency oscillations and resonance analysis of VSG-controlled PMSG-based wind generation systems," *Journal of Modern Power Systems and Clean Energy*, vol. 13, no. 1, pp. 115-127, Jan. 2025.
- [7] Z. Wang, Y. Wang, M. Davari *et al.*, "An effective PQ -decoupling control scheme using adaptive dynamic programming approach to reducing oscillations of virtual synchronous generators for grid connection with different impedance types," *IEEE Transactions on Industrial Electronics*, vol. 71, no. 4, pp. 3763-3775, Apr. 2024.
- [8] Z. Meng, X. Xing, X. Li *et al.*, "Compound compensation control for improving low-voltage ride-through capability of virtual synchronous generators," *Journal of Modern Power Systems and Clean Energy*, vol. 13, no. 3, pp. 1064-1077, May 2025.
- [9] A. E. Leon and J. M. Mauricio, "Virtual synchronous generator for VSC-HVDC stations with DC voltage control," *IEEE Transactions on Power Systems*, vol. 38, no. 1, pp. 728-738, Jan. 2023.
- [10] A. E. Leon and J. M. Mauricio, "Virtual synchronous generator for VSC-HVDC stations with DC voltage control," *IEEE Transactions on Power Systems*, vol. 38, no. 1, pp. 728-738, Jan. 2023.
- [11] Q. Zhang, Y. Li, Z. Ding *et al.*, "Self-adaptive secondary frequency regulation strategy of micro-grid with multiple virtual synchronous generators," *IEEE Transactions on Industry Applications*, vol. 56, no. 5, pp. 6007-6018, Sept. 2020.
- [12] F. J. Matas-Díaz, M. Barragán-Villarejo, and J. M. Maza-Ortega *et al.*, "A systematic small-signal analysis procedure for improving synchronization stability of grid-forming virtual synchronous generators," *Journal of Modern Power Systems and Clean Energy*, vol. 13, no. 1, pp. 102-114, Jan. 2025.
- [13] S. Zou, W. Zhao, C. Wang *et al.*, "Tracking and synchronization control strategy of vehicle dual-motor steer-by-wire system via active disturbance rejection control," *ASME Transactions on Mechatronics*, vol. 28, no. 1, pp. 92-103, Feb. 2023.
- [14] C. Sun, C. Liu, X. Feng *et al.*, "Visual servoing of flying robot based on fuzzy adaptive linear active disturbance rejection control," *IEEE Transactions on Circuits and Systems II: Express Briefs*, vol. 68, no. 7, pp. 2558-2562, Jul. 2021.
- [15] H. Wang, J. Deng, L. Zhang *et al.*, "Enhanced disturbance observer-based hybrid cascade active disturbance rejection control design for high-precise tracking system in application to aerospace satellite," *Aerospace Science and Technology*, vol. 146, p. 108939, Mar. 2024.
- [16] J. Li, Y. Xia, X. Qi *et al.*, "Robust absolute stability analysis for interval nonlinear active disturbance rejection based control system," *ISA Transactions*, vol. 69, pp. 122-130, Jul. 2017.
- [17] B. Peng, N. Gu, D. Wang *et al.*, "Model-free adaptive disturbance rejection control of an rsv with hardware-in-the-loop Experiments," *IEEE Transactions on Industrial Electronics*, vol. 70, no. 7, pp. 7507-7510, Jul. 2023.
- [18] H. Wang, T. Pan, and G. Chen, "Discrete active disturbance rejection control for semiconductor manufacturing processes with dynamic models," *IEEE Transactions on Semiconductor Manufacturing*, vol. 36, no. 4, pp. 636-644, Nov. 2023.
- [19] N. Elghardouf, Y. Ennaciri, A. Elakkary *et al.*, "Multi-loop active disturbance rejection control and PID control strategy for poultry house based on GA, PSO and GWO algorithms," *Heliyon*, vol. 10, no. 8, p. e29579, Apr. 2024.
- [20] H. Jie, G. Zheng, J. Zou *et al.*, "Speed regulation based on adaptive control and RBFNN for PMSM considering parametric uncertainty and load fluctuation," *IEEE Access*, vol. 8, pp. 190147-190159, Jan. 2020.
- [21] M. Ge, Q. Song, X. Hu *et al.*, "RBFNN-based fractional-order control of high-speed train with uncertain model and actuator failures," *IEEE Transactions on Intelligent Transportation Systems*, vol. 21, no. 9, pp. 3883-3892, Sept. 2020.
- [22] A. F. Rashwan, M. Ahmed, M. R. Mossa *et al.*, "Explicit adaptive power system stabilizer design based on an on-line identifier for single-machine infinite bus," *Ain Shams Engineering Journal*, vol. 13, no. 2, p. 101544, Mar. 2022.
- [23] A. Hamim, N. I. M. Yusoff, H. A. Omar *et al.*, "Integrated finite element and artificial neural network methods for constructing asphalt concrete dynamic modulus master curve using deflection time-history data," *Construction and Building Materials*, vol. 257, p. 119549, Oct. 2020.
- [24] C. Wang, X. Li, J. Zhang *et al.*, "A modified radial basis function network integrating Mahalanobis distance and LASSO for soil mapping," *Ecological Informatics*, vol. 77, p. 102279, Nov. 2023.
- [25] D. Zhang, N. Zhang, N. Ye *et al.*, "Hybrid learning algorithm of radial basis function networks for reliability analysis," *IEEE Transactions on*

- Reliability*, vol. 70, no. 3, pp. 887-900, Sept. 2021.
- [26] J. Chen, C. Fang, X. Zhang *et al.*, "A radial basis function-based graph attention network with squeeze loss optimization for link prediction," *IEEE Transactions on Artificial Intelligence*, vol. 5, no. 2, pp. 724-736, Feb. 2024.
- [27] G. Tuccio, S. Afrakhteh, G. Iacca *et al.*, "Time efficient ultrasound localization microscopy based on a novel radial basis function 2D interpolation," *IEEE Transactions on Medical Imaging*, vol. 43, no. 5, pp. 1690-1701, May 2024.
- [28] C. Wang, A. Wang, S. Chen *et al.*, "Optimal operation of microgrids based on a radial basis function metamodel," *IEEE Systems Journal*, vol. 16, no. 3, pp. 4756-4767, Sept. 2022.
- [29] J. Wang, N. Ramli, and N. H. A. Aziz, "Pre synchronization control strategy of virtual synchronous generator (VSG) in micro-grid," *IEEE Access*, vol. 11, pp. 139004-139016, Sept. 2023.
- [30] Y. Dai, L. Zhang, Q. Chen *et al.*, "Multi-VSG-based frequency regulation for uninterruptible power AC micro-grid with distributed electric vehicles," *International Journal of Electrical Power & Energy Systems*, vol. 137, p. 107785, May 2022.
- [31] K. Feng and C. Liu, "Distributed hierarchical control for fast frequency restoration in VSG-controlled islanded microgrids," *IEEE Open Journal of the Industrial Electronics Society*, vol. 3, pp. 496-506, Aug. 2022.
- [32] G. Lou, Q. Yang, W. Gu *et al.*, "An improved control strategy of virtual synchronous generator under symmetrical grid voltage sag," *International Journal of Electrical Power & Energy Systems*, vol. 121, p. 106093, Oct. 2020.
- [33] A. Malkhandi, N. Senroy, and S. Mishra, "A dynamic model of impedance for online thevenin's equivalent estimation," *IEEE Transactions on Circuits and Systems II: Express Briefs*, vol. 69, no. 1, pp. 194-198, Jan. 2022.
- [34] R. Luhtala, T. Roinila, and T. Messo, "Implementation of real-time impedance-based stability assessment of grid-connected systems using MIMO-identification techniques," *IEEE Transactions on Industry Applications*, vol. 54, no. 5, pp. 5054-5063, Sept. 2018.
- [35] C. Li, Y. Yang, and F. Blaabjerg, "Mechanism analysis for oscillation transferring in grid-forming virtual synchronous generator connected to power network," *IEEE Transactions on Industrial Electronics*, vol. 72, no. 8, pp. 8715-8720, Aug. 2025..
- [36] S. de L. Diz, R. M. Lopez, F. J. R. Sanchez *et al.*, "A digital twin approach for online impedance-based stability analysis of three-phase AC systems," *IEEE Transactions on Industrial Electronics*, vol. 71, no. 12, pp. 16845-16856, Dec. 2024.
- [37] R. Hassan, H. Wang, and R. Zane, "A new online continuous stability monitoring method for DC microgrids," *IEEE Transactions on Power Electronics*, vol. 38, no. 9, pp. 10739-10749, Sept. 2023.
- [38] W. Tahir, M. Farhan, A. R. Bhatti *et al.*, "A modified control strategy for seamless switching of virtual synchronous generator-based inverter using frequency, phase, and voltage regulation," *International Journal of Electrical Power & Energy Systems*, vol. 157, p. 109805, Jun. 2024.
- [39] L. Chen, M. Ding, Z. Li *et al.*, "Coordination of adaptive virtual resistance controller and flux-coupling-type fault current limiter for LVRT fulfillment of virtual synchronous generator," *Electric Power Systems Research*, vol. 210, p. 108112, Sept. 2022.
- [40] C. Zhou, Z. Li, G. Cui *et al.*, "Finite-time secondary frequency modulation of microgrid based on event triggering mechanism," *International Journal of Control, Automation and Systems*, vol. 22, no. 4, pp. 1252-1263, Mar. 2024.
- [41] H. Wan, X. Qi, and J. Li, "Stability analysis of linear/nonlinear switching active disturbance rejection control based MIMO continuous systems," *Journal of Systems Engineering and Electronics*, vol. 32, no. 4, pp. 956-970, Aug. 2021.
- [42] Z. Wu, F. Deng, B. Guo *et al.*, "Backstepping active disturbance rejection control for lower triangular nonlinear systems with mismatched stochastic disturbances," *IEEE Transactions on Systems, Man, and Cybernetics: Systems*, vol. 52, no. 4, pp. 2688-2702, Apr. 2022.
- [43] K. Li, G. Cheng, X. Sun *et al.*, "Direct torque and suspension force control for bearingless induction motors based on active disturbance rejection control scheme," *IEEE Access*, vol. 7, pp. 86989-87001, Jun. 2019.
- [44] Z. Liu, Y. Chen, Z. Zhang *et al.*, "Identification of vulnerable nodes and sensitivity analysis of control parameters for multiple grid-connected converter systems," *IEEE Transactions on Sustainable Energy*, vol. 16, no. 3, pp. 1602-1612, Jul. 2025.

Yangyang Chen received the B.Eng. degree in electrical engineering and automation from Hainan University, Haikou, China, in 2019, and the M.Sc. degree in electrical and electronic engineering from The University of Hong Kong, Hong Kong, China, in 2021. He is currently working toward the Ph.D. degree in sustainable energy and environment thrust with The Hong Kong University of Science and Technology (Guangzhou), Guangzhou, China. His research interests include power electronics, adaptive dynamic programming, optimal control of linear system, and control of power system.

Wei Han received the M.Sc. and Ph.D. degrees in electrical and electronic engineering from The University of Hong Kong, Hong Kong, China, in 2015 and 2020, respectively. In 2021, he was a Postdoctoral Fellow at the University of Toronto, Toronto, Canada. He is currently an Assistant Professor in The Hong Kong University of Science and Technology (Guangzhou), Guangzhou, China. He is also an Affiliated Assistant Professor with the Department of Electronic & Computer Engineering, The Hong Kong University of Science and Technology, Hong Kong, China. His research interests include power electronics, wireless power transfer, electric motor drive, and microgrid.

Youhao Hu received the M.Sc. degree in electrical and electronics engineering from Hefei University of Technology, Hefei, China, in 2019. He is currently working toward the Ph.D. degree in sustainable energy and environment thrust with The Hong Kong University of Science and Technology (Guangzhou), Guangzhou, China. His research interests include power electronics, wireless power transfer, nonlinear system, and sliding mode control.

Hanlei Tian received the M.Sc. degree from the University of Science and Technology of Hebei, Shijiazhuang, China, in 2016. From 2016 to 2019, he was a Cocultured Student with the Electric Power College, South China University of Technology, Guangzhou, China. From 2019 to 2022, he worked toward the Ph.D. degree with the Electrical Engineering School of Sichuan University, Chengdu, China. He is currently working toward the Ph.D. degree in sustainable energy and environment thrust, The Hong Kong University of Science and Technology (Guangzhou), Guangzhou, China. His research interests include high-frequency power converter, renewable energy conversion system, grid-connected converter, and modeling and control of converter.

Yilin Zhang received the B.Eng degree in electrical engineering and automation from Xi'an Jiaotong University, Xi'an, China, in 2022, and the M.Sc. degree in electronic information engineering from City University of Hong Kong, Hong Kong, China, in 2023. He is currently working toward the Ph.D. degree in sustainable energy and environment thrust with The Hong Kong University of Science and Technology (Guangzhou), Guangzhou, China. His research interests include wireless power transfer and electric motor drive.

Junyu Fan received the B.Eng degree in electrical engineering and automation from Dalian Maritime University, Dalian, China, and the M.Sc. degree in electronic information from Southeast University, Nanjing, China. He is currently working toward the Ph.D. degree in sustainable energy and environment thrust, Hong Kong University of Science and Technology (Guangzhou), Guangzhou, China. His research interests include control and analysis of ultrasonic motor and wireless power transfer.